

Influence of chemical solution growth and vacuum annealing on the properties of (100) pseudocubic oriented BiFeO₃ thin films

Cite as: J. Appl. Phys. **126**, 135303 (2019); <https://doi.org/10.1063/1.5110588>

Submitted: 22 May 2019 . Accepted: 17 September 2019 . Published Online: 03 October 2019

Subhajit Nandy, and C. Sudakar 



View Online



Export Citation



CrossMark

ARTICLES YOU MAY BE INTERESTED IN

Structure, electrical and magnetic properties of Co_{0.8}Zn_{0.2}Fe₂O₄/(K_{0.47}Na_{0.47}Li_{0.6}) NbO₃ bilayered thin films grown by pulsed laser deposition

Journal of Applied Physics **126**, 134104 (2019); <https://doi.org/10.1063/1.5095188>

Analysis and control of heating of magnetic nanoparticles by adding a static magnetic field to an alternating magnetic field

Journal of Applied Physics **126**, 134902 (2019); <https://doi.org/10.1063/1.5097415>

Interrogating the impact of onion-like carbons on the supercapacitive properties of MXene (Ti₂CT_x)

Journal of Applied Physics **126**, 134301 (2019); <https://doi.org/10.1063/1.5112107>

Ultra High Performance SDD Detectors



See all our XRF Solutions

Influence of chemical solution growth and vacuum annealing on the properties of (100) pseudocubic oriented BiFeO₃ thin films

Cite as: J. Appl. Phys. **126**, 135303 (2019); doi: [10.1063/1.5110588](https://doi.org/10.1063/1.5110588)

Submitted: 22 May 2019 · Accepted: 17 September 2019 ·

Published Online: 3 October 2019



Subhajit Nandy and C. Sudakar^{a)}

AFFILIATIONS

Multifunctional Materials Laboratory, Department of Physics, Indian Institute of Technology Madras, Chennai 600036, India

^{a)}Author to whom correspondence should be addressed: csudakar@iitm.ac.in

ABSTRACT

BiFeO₃ (BFO), a Pb-free perovskite oxide, is being explored for its potential use in a multitude of applications. We report on the oriented growth of BFO thin films using a facile metal-organic chemical solution deposition. Unlike the growth characteristics observed in Si/SiO₂ and glass/FTO substrates, the solution growth process on sapphire (0001) is found to yield highly oriented thin films along (100)_{pc} planes. Furthermore, annealing in air (BFO-A) and high-vacuum (BFO-V) ambients are done to explore the tunable limits of its physical properties. Temperature-dependent Raman studies highlight the high quality of thin films with sharp changes in Raman modes around transition temperatures. In addition, the films exhibit a hitherto unreported anomalous shift in A₁(TO) and E(TO) modes around 450 K. The bandgap of BFO-V (E_g = 2 eV) is lower than that of BFO-A (E_g = 2.12 eV) and exhibits an increased defect photoluminescence emission. The magnetization (M) is twofold higher for BFO-V [$M \approx 42$ (67) emu/cm³ at 300 K (5 K)]. In-plane and out-of-plane M vs H plots show larger anisotropy and hard hysteresis for BFO-A compared to BFO-V. Piezoelectric switching with d_{33} values of 5–10 pm/V is the characteristic of BFO ferroelectric materials. Photoconductivity measurements show a one order increase due to vacuum annealing. Carrier generation and recombination lifetimes are twofold faster in BFO-V as compared to BFO-A thin films. The controllable physical properties of oriented BiFeO₃ thin films will be useful in magnetoelectrics and photoferroelectrics applications.

Published under license by AIP Publishing. <https://doi.org/10.1063/1.5110588>

I. INTRODUCTION

BiFeO₃ is a rhombohedrally distorted perovskite type material which belongs to the *R3c* space group. It has been widely studied as a room temperature single phase multiferroic material with a ferroelectric Curie temperature of 1103 K and a magnetic Néel transition temperature of 643 K.¹ A BiFeO₃ thin film with a narrow bandgap (2.1–2.7 eV) has attracted intensive attention due to its excellent multifunctional properties and as a Pb-free perovskite.² These include multiferroism,^{3,4} resistive switching,^{5,6} high open circuit voltage in photovoltaic devices,⁷ photocatalysis,^{8,9} and photoelectrochemical¹⁰ properties. A strong coupling between structural, ferroelectric, magnetic, and optical properties project BiFeO₃ has a unique multifunctional material for various device applications including multiferroics,¹¹ electronics,¹² spintronics,¹³ photovoltaics,^{14,15} and photonics.¹⁶ Continued research interest prevails due to this for understanding the physical properties of high quality or epitaxially grown thin films.^{4,17–19} Until now various advanced

deposition techniques have been employed to obtain epitaxial BiFeO₃ films. These include pulsed laser deposition,^{4,20} radiofrequency magnetron sputtering,^{21,22} molecular beam epitaxy,^{23,24} and metal-organic chemical vapor deposition.^{25,26}

Chemical solution deposition (CSD) is an alternative approach to prepare oxide thin films. Many functional materials have been successfully fabricated using the CSD technique.^{27–29} However, chemical solutions and growth conditions used vary largely among these reports. The method has several advantages, such as control on stoichiometry, ease of fabrication on large area, wide variety of substrates, and low cost production. On the other hand, it is shown that obtaining high quality epitaxial BiFeO₃ thin films via CSD is challenging. Structural, magnetic, and ferroelectric properties of polycrystalline BiFeO₃ thin films prepared using CSD on Pt/Ti/SiO₂/Si(100) and Pt/sapphire(0001) substrates have been reported.^{30,31} Naganuma and Okamura³⁰ have shown a high remanent polarization of 47 μC/cm² at room temperature in polycrystalline

BiFeO₃ films grown on the Pt/Ti/SiO₂/Si(100) substrate. Singh *et al.*³¹ have observed an improved remanent polarization of 100 $\mu\text{C}/\text{cm}^2$ in polycrystalline BiFeO₃ films grown on the Pt/sapphire(0001) substrate at 80 K compared to the films grown on the Pt/Ti/SiO₂/Si(100) substrate. This result was attributed to an improved BiFeO₃/Pt interface on the sapphire substrate. Highly oriented or epitaxially grown BiFeO₃ thin films using CSD on different substrates have also been reported.^{32–36} The magnetic property of oriented BiFeO₃ films deposited on LaAlO₃ (001) substrates shows a large saturation magnetization of $\sim 250 \text{ emu}/\text{cm}^3$ when annealed in oxygen at 550 °C for 1 h.³² Epitaxial rhombohedral BiFeO₃ thin films fabricated by CSD on (001), (110), (111) single crystal SrRuO₃/SrTiO₃ substrates were reported by Singh *et al.*³³ BiFeO₃ (001) thin films were found to exhibit a maximum remanent polarization of 50 $\mu\text{C}/\text{cm}^2$ at 80 K.³³ Tyholdt *et al.*³⁴ have synthesized (012)_R oriented BiFeO₃ epitaxial films of a thickness of 120 nm via CSD on MgO(100)/Pt(100) substrates. This study shows a careful control of excess Bi used for counterbalancing the evaporation during crystallization. Ferroelectric, dielectric, and resistive switching behaviors were investigated by Zhang *et al.*³⁶ on (001)_{pc} oriented BiFeO₃ thin films of various thicknesses deposited on the La_{0.67}Sr_{0.33}MnO₃ buffered (001) SrTiO₃ substrate.³⁶ Highest remanent polarization ($2P_r = 100 \mu\text{C}/\text{cm}^2$) and relative dielectric constant ($\epsilon_r = 613$) at room temperature observed at a frequency of 1 MHz of a 150 nm thick BiFeO₃ film were attributed to the combined effect of substrates, buffer layers, and BiFeO₃ films.

Single crystalline epitaxial thin films of BiFeO₃ are useful for photovoltaic and photodetector applications.^{37,38} The planar configuration of ferroelectric photovoltaic (FE-PV) devices, in which two contacts made on the top surface of films are used to test PV device characteristics, is found to exhibit high voltage due to the ferroelectric nature of films.³⁹ This device configuration is also found to be advantageous over the commonly used in-plane capacitor devices, as the latter is more prone to get short circuited due to the presence of defects like pinholes in the films. Similarly, devices having preferential growth features with the coplanar electrode configuration are of use in highly sensitive and fast response photodetector applications.³⁸ Methods including MBE,²⁴ PLD,⁴ and MOCVD⁴⁰ have been used to fabricate epitaxial BFO thin films. However, it is important to develop procedures to fabricate epitaxial and/or highly oriented thin films by a simple solution growth process and understand the physical properties of such films to realize their relevance to various other applications.

There is a significant interest to grow thin films on different substrates including FTO, Si/SiO₂, and sapphire substrates. In fact, growth conditions including the substrates significantly influence thin film quality, specifically, when approaches such as simple facile solution growth process are used. In our group, we found that films grown on the sapphire (0001) substrate are to be highly oriented. This calls for fabricating BiFeO₃ thin films to realize growth conditions of oriented BiFeO₃ crystallites using sapphire as a substrate and investigating the properties by the simple solution growth process. It is also important to tailor the chemical composition, specifically oxygen stoichiometry, to control the physical properties. Oxygen vacancies introduced by the vacuum annealing process are being used to control the oxygen stoichiometry, more prominently in bulk samples.^{41–43} Oxygen vacancies reduce activation

energy and lead to increased conductivity without imposing large structural changes in the BiFeO₃ sample.⁴³ Thus, the advantages of growing oriented thin films as well as controlling oxygen stoichiometry to change the physical properties can be exploited for a wide range of applications.

To our knowledge, there are no reports of (100)_{pc} oriented BiFeO₃ thin films grown directly on sapphire (0001) substrates with or without buffer layers. In this paper, we present the structural properties of highly oriented BiFeO₃ thin films prepared using a simple chemical solution deposition technique which involves spin coating of a metal-organic precursor solution. Annealing process dependent structural and physical properties are investigated. Structural, optical, piezoforce microscope images, magnetic properties, and photoconductivity studies on these oriented BiFeO₃ thin films grown on the sapphire substrate are presented. Air and vacuum annealed BiFeO₃ thin films, grown on sapphire, are useful for in-plane photovoltaic and photodetector applications.

II. EXPERIMENTAL

BiFeO₃ (BFO) thin films were prepared by the metal-organic chemical solution deposition technique.⁴⁴ Bismuth 2-ethylhexanoate (C₂₄H₄₅BiO₆) and iron (III) 2-ethylhexanoate (C₂₄H₄₅FeO₆) were used as precursors in a 1:1 molar ratio and *O*-xylene was used as a solvent (50 wt. %). Precursors were taken in a cleaned bottle and the solvent was added to it. Sapphire (0001) substrates were cleaned by ultrasonication in ethanol and acetone for 15 min each. Before using the substrate, the surface was blown with N₂ gas and dried with a hot air gun. The solution is coated on cleaned sapphire substrates using the spin coating technique. The precursor solution ($\sim 50 \mu\text{l}$) was dropped and the sapphire substrate was spun at a speed of 2000 rpm for 20 s. The coated layer was heated at 400 °C for 2 min to remove the solvent. This procedure is repeated for building thick layers of coating. Typically, five layers were coated for all the samples. The concentration of the solution and the number of coatings are optimized to obtain the same thickness. Final annealing was done at 550 °C for 1 h in air. This sample is labeled BFO-A. Furthermore, BFO-A thin films are annealed in high vacuum (8×10^{-6} Torr) at 450 °C for 2 h. This sample is referred to as BFO-V.

X-ray diffraction (XRD) patterns of BFO thin films were recorded using a X'Pert-Pro, Panalytical power diffractometer using Cu-K α radiation ($\lambda = 1.5406 \text{ \AA}$) to investigate the phase and crystallinity of BFO thin films. Field emission scanning electron microscopy (FESEM) was carried out using Inspect F, FEI microscope for morphological studies. Raman spectra were acquired with a He-Ne laser of wavelength 632 nm (red laser) using a Horiba Jobin-Yvon (HR800 UV) micro-Raman spectrometer to confirm the phase purity. Temperature-dependent Raman studies were carried out on BFO-A and BFO-V thin films to understand the influence of oxygen vacancy on the magnetic transition temperature. Optical properties of BFO films were carried out using the Bentham PVE300 integrating sphere configuration for wavelengths ranging from 300 nm to 1750 nm. Photoluminescence spectra were collected using Ar ion laser of wavelength 488 nm (blue laser) from a Horiba Jobin-Yvon (HR800 UV) micro-Raman spectrometer. Ferroelectric domains were imaged by a piezoforce microscope

using the NX10 Park system. To study the magnetic property of BFO thin films, M-H hysteresis curves were acquired by applying magnetic field up to ± 7 T. ZFC-FC measurements with an applied magnetic field of 500 Oe were also carried out using a Quantum Design SQUID vibrating sample magnetometer. To study the photoconductivity measurements on BFO thin films, Au pattern stripes of 1 mm width and 5 mm length with 1 mm gap were coated on films using the radiofrequency magnetron sputter deposition technique at a chamber pressure of 2×10^{-2} mbar for 1 min. Applying a constant current using a Keithley 2400 source meter, the change in the voltage is monitored under dark and AM 1.5 one Sun illumination (100 mW/cm^2) to study the photoconductivity measurements. All the photoconductivity measurements are carried out at room temperature.

III. RESULTS AND DISCUSSION

Powder x-ray diffraction patterns of BFO thin films on the sapphire substrate are shown in Fig. 1(a). Both the films (BFO-A and BFO-V) show strong reflections at $2\theta \approx 22.5^\circ$ and $\approx 45.8^\circ$, which are attributed to the $(100)_{\text{pc}}/(012)_{\text{R}}$ and $(200)_{\text{pc}}/(024)_{\text{R}}$ lines of the pseudocubic/rhombohedral BFO phase. These peaks are oriented strongly along the sapphire substrate's (0001) plane, indicating $[100]_{\text{pc}}$ directed preferential growth of BFO films normal to the substrate surface. The full width half maximum (FWHM) from these strong peaks is a bit broad suggesting nanoparticulate nature of grains. Average particle size corresponding to BFO-A and

BFO-V thin films estimated using the Scherrer equation are 27 nm and 28 nm, respectively. A double peak around 32° with lesser intensity compared to that of $(100)_{\text{pc}}$ peak corresponds to $(110)_{\text{pc}}/ (104)_{\text{R}}$ and $(-110)_{\text{pc}}/(110)_{\text{R}}$ reflections of BFO phase. Other small peaks observed at $2\theta \approx 52^\circ$ and 57° , decipherable when the intensity is plotted in log scale, correspond to $(210)_{\text{pc}}$ and $(211)_{\text{pc}}$ planes, respectively. Liu *et al.* have also shown the presence of a low intense double peak at $2\theta \sim 32^\circ$ for $(100)_{\text{pc}}$ oriented BiFeO_3 films grown by the sol gel method on the Pt/Ti/SiO₂/Si substrate.⁴⁵

Rocking curves of the peaks $(100)_{\text{pc}}$ and $(200)_{\text{pc}}$ are shown in Figs. 1(b) and 1(c). FWHM in rocking curve is a parameter to measure the quality of oriented nature crystallites in the films. Usually, epitaxial films show low values ($\sim 0.6^\circ$) of FWHM.⁴⁶ Highly oriented crystallites would exhibit more broadening. For BFO-A thin films, FWHM is found to be 8.4° and 8.3° for $(100)_{\text{pc}}$ and $(200)_{\text{pc}}$ reflections suggesting that the crystallite orientation is broadly distributed from the perpendicular direction, i.e., the crystallites are slightly off from the perpendicular direction of the substrate surface. Tyholdt *et al.* have shown FWHM values of 10% Bi-excess $(012)_{\text{R}}$ oriented rhombohedral BFO thin films crystallized at 600°C and 700°C to be 6.6° and 6.2° , respectively.³⁵ Vacuum annealing of BFO-A thin films (BFO-V) has led to a reduction in the FWHM from 8.4° to 6.7° for $(100)_{\text{pc}}$ peak and 8.3° to 5.9° for $(200)_{\text{pc}}$ peak. However, it should be noted that the air-annealing was carried out for 1 h, whereas vacuum annealing was performed for 2 h in addition to 1 h air-annealing. Annealing for a longer time could improve the crystallinity and oriented nature. To check this, we carried out the annealing of BFO-A thin films for 3 h (Fig. S1 in the supplementary material). The XRD patterns show improvements in the crystallinity as inferred from the decreasing FWHM. The FWHM estimated from rocking curves of $\{100\}$ planes exhibit values from $\sim 7.1^\circ$ to 7.3° , which are lower than those of BFO-A films annealed for 1 h (FWHM $\sim 8.4^\circ$). However, we found that the microstructure was intact, and no discernible changes were found due to prolonged annealing. The SEM images of BFO-A samples annealed for 1 h and 3 h are given in Fig. S2 (supplementary material).

To ascertain the role of substrates, we have grown BiFeO_3 thin films on Si/SiO₂, Si/SiO₂/Pt, and glass/FTO substrates and annealed them under the same condition (at 550°C for 1 h). The XRD patterns of all these films are provided in Fig. S3 (supplementary material). The data are shown in comparison to the films grown on sapphire. BiFeO_3 coated on Si/SiO₂, Si/SiO₂/Pt, and glass/FTO substrates show XRD profiles corresponding to a polycrystalline BiFeO_3 with no indications of oriented growth features of crystallites. Thus, the growth of BiFeO_3 thin films is highly influenced by the substrate and sapphire yields oriented BFO, whereas, the growth of BFO on Si/SiO₂, Si/SiO₂/Pt, and glass/FTO substrates resulted in polycrystalline films. In this work, we focus on the properties of oriented BFO films grown on sapphire substrates.

FESEM images depicting the surface topography and cross-section of BFO-A and BFO-V films coated on the sapphire substrate are shown in Fig. 2. Grain sizes of 50 nm to 150 nm are observed in both the films. Tiny pores are seen in between grains. In most of the places, grains are fused together to form a continuous surface connectivity. In between, the pore regions and mostly along the grain boundaries nanometer sized particles are seen.

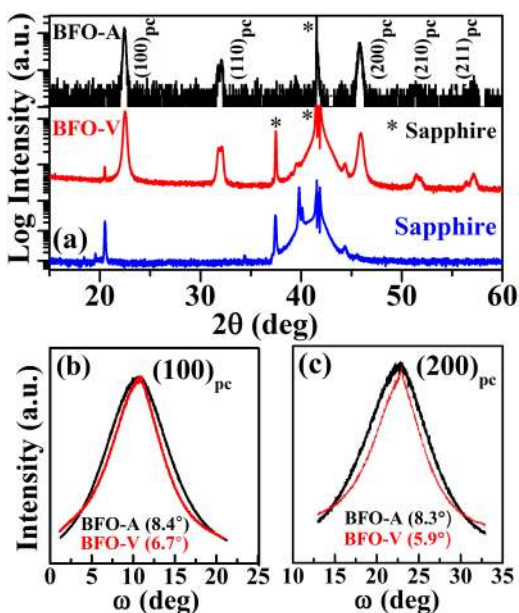


FIG. 1. (a) X-ray diffraction (XRD) patterns of the air-annealed BiFeO_3 (BFO-A) and the vacuum annealed BiFeO_3 (BFO-V) thin films coated on a sapphire (0001) substrate. XRD pattern of single crystal sapphire substrate is also shown in (a). (b) and (c) are the rocking curves of $(100)_{\text{pc}}$ and $(200)_{\text{pc}}$ diffraction peak for both the samples.

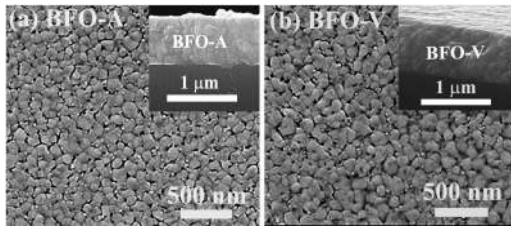


FIG. 2. FESEM images of the surface topography of (a) BFO-A and (b) BFO-V thin films on the sapphire substrate. Cross-sectional view of the films are shown in the insets of (a) and (b) for the corresponding film.

These particles are found to decrease and disappear on vacuum annealing with a consequent increase in the connectivity among the grains. The cross-sectional SEM images show the thickness of BFO-A and BFO-V thin films [Figs. 2(a) and 2(b)] and they are in the range of 600 to 700 nm. Furthermore, the porous regions seen in the surface topography do not extend down to the substrate. Thus, the films are devoid of any pinholes. The morphology of particles in BFO-V does not get altered except for the fusing of particles along the grain boundaries and disappearance of some of the nanoparticles in between the pore region.

The quality of thin films and structural changes due to vacuum annealing are investigated using temperature-dependent Raman spectral studies. Raman spectra acquired at 123 K from BFO-A and BFO-V films show modes corresponding to the phase pure BiFeO₃ composition (Fig. 3). The spectra are fitted with Lorentzian-Gaussian profiles and the fitted curves along with the deconvoluted components are shown in Figs. 3(a) and 3(c). First two strong modes observed at $\sim 147\text{ cm}^{-1}$ and $\sim 176\text{ cm}^{-1}$ (which appear at $\sim 141\text{ cm}^{-1}$ and $\sim 173\text{ cm}^{-1}$, respectively, at 300 K in the spectra) in BFO-A indicate the E(TO) modes corresponding to the Bi-O vibrations.^{47,48} These modes are typical of spectral features reported for BFO single crystal and several tens of micrometer-sized bulk samples.⁴⁷ The A₁(TO) modes which are reported to be more prominent compared to the E(TO) modes in the smaller sized (<65 nm) crystallites are not intense in BFO-A and BFO-V thin films.⁴⁸ Thus, despite the nanocrystalline nature of grains with size in the range of 50 nm to 150 nm, the strong E(TO) vibrational modes further substantiate the high crystalline quality of the BiFeO₃ structure. A slight blue shift in the A₁(TO) and E(TO) peak positions is found in the BFO-V thin films at room temperature. This blue shift observed in A₁(TO) and E(TO) modes of BFO-V thin films is attributed to the altered Bi-O and Fe-O-Fe bond parameters due to the formation of oxygen vacancies on vacuum annealing. The formation of oxygen vacancies (O_V) in BFO-V films affects the vibrational modes of M-O-M bonds by way of changes in the oxygen bonding, thus resulting into a slight shift in Raman spectral modes. Structural instabilities due to temperature and pressure are common in perovskite materials like BiFeO₃. Several reports have explored the chemical pressure effects, mostly caused by the dopants on the physical properties.^{44,49,50} However, investigations on the effect of introduction of oxygen vacancy are scarce. Fewer reports suggest that oxygen vacancy related disorder generally tends to blue shift the Raman modes.⁵¹

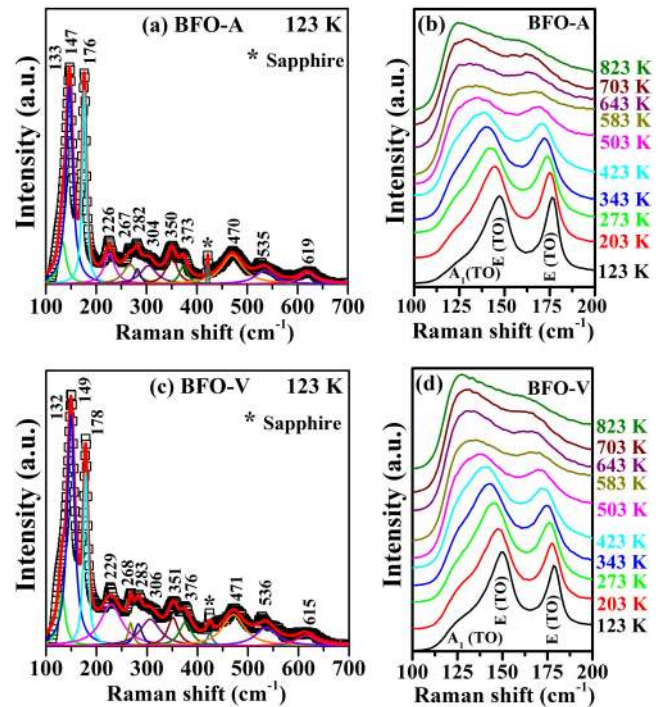


FIG. 3. Raman spectra of (a) and (b) BFO-A and (c) and (d) BFO-V thin films fabricated on the sapphire (0001) substrate and measured at various temperatures between 123 K and 823 K. (a) and (c) Raman spectra of BFO thin films measured at 123 K; open square symbol represents the experimental data, red line shows the total fit, and other colored lines show the deconvoluted curves. (b) and (d) Temperature-dependent Raman spectra in the range between 100 and 200 cm^{-1} are shown which mainly highlight the change in the peak position for first three modes [A₁(TO), and two E(TO)].

Figures 3(b) and 3(d) show the temperature-dependent variation of A₁(TO) and E(TO) Raman modes spectra in BFO-A and BFO-V films. Raman spectra were collected over a temperature range 123 K to 823 K. The temperature-dependent changes in the peak positions of these modes are presented in Fig. 4. With increasing temperature Raman modes shift to lower frequencies and the peaks broaden. This red shift and peak broadening can be attributed to the thermally disturbed phonons and lattice expansion due to anharmonic effects.⁵² Interestingly, we observe that the position of A₁(TO) mode $\sim 135\text{ cm}^{-1}$ (from spectra acquired at 123 K) decreases rapidly as the temperature increases from 123 K to 300 K. On the other hand, the E(TO) mode position show slow linear decrease up to 400 K. At all the temperatures, the position of these vibrational modes in BFO-V is found to be slightly more than those obtained for BFO-A thin films. Another interesting feature we observe is the appearance of two anomalies at 463 K and 663 K in the peak position vs temperature plots shown for A₁(TO) and E(TO) modes (Fig. 4). Since we do not see any additional modes in the spectra with temperature change, these anomalies cannot be related to any structural variations or secondary phase formation and can be mostly attributed to the spin-phonon coupling.

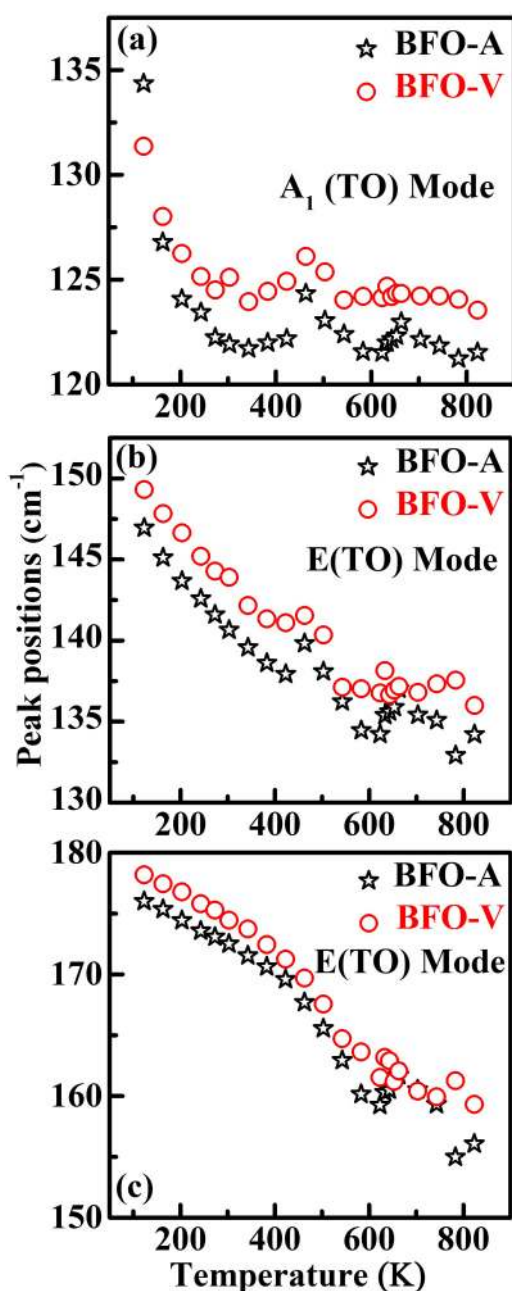


FIG. 4. Temperature-dependent shift in Raman peak positions of (a) $A_1(\text{TO})$ mode and (b) and (c) $E(\text{TO})$ modes of BFO-A and BFO-V films.

The anomaly seen in the temperature range of 623–663 K is near the antiferromagnetic to paramagnetic transition ($T_N \sim 643$ K) and hence attributed to spin-phonon interaction. Similar phonon anomaly coinciding with the magnetic phase transitions were reported earlier in many oxides and are attributed to a strong

electron-phonon coupling in those systems.⁵³ The local spin correlations get perturbed near T_N bringing in very weak structural instabilities due to the spin-spin interactions.⁵³ This leads to an enhanced spin-phonon coupling and changes in the modes involving M–O–M bond angle and thereby explains the observed fluctuations in the peak position.

The anomaly in the temperature range of 383–463 K seen as a sudden increase in the peak position is observed for $A_1(\text{TO})$ and one of the $E(\text{TO})$ modes (~ 150 cm^{-1}). However, for the second $E(\text{TO})$ mode (~ 180 cm^{-1}), we observe a rapid fall in the peak position values in the temperature range from 383 to 463 K. Most of the temperature-dependent anomalies reported earlier on BiFeO_3 ceramic and thin films were seen in the low temperature region.^{54–59} These reported anomalies are summarized in Table S1 of the [supplementary material](#). Most of these anomalies were attributed either to a local structural rearrangement or to a magnetic phase transition other than Néel transition. Spin reorientation⁵⁶ and magnon-phonon coupling⁵⁷ related anomalies were reported in the low frequency (<65 cm^{-1}) Raman modes. The anomaly observed at ~ 460 K in this work does not match with any of those reported either on single crystal BiFeO_3 or nanocrystalline samples. Since this anomaly is seen both in BFO-A and BFO-V specimens with similar strength, it indicates that O_V has no significant role. However, the surface structure in nanomaterials forms a large mass fraction of the material, and therefore any local structural changes near the surface can result in such an anomaly. These changes can be due to large interfacial strains percolating into the nanoparticle cores or Bi ion deficiency due to high volatility.⁶⁰ We speculate that any spin related change with strong phonon coupling on the surface could have caused such anomaly. Duan *et al.*⁵⁸ reported a very weak anomaly ~ 500 K on BFO grown on *c*-sapphire and they have attributed it to the phase transition from one state of ferroelectric ordering to another associated with Bi^{3+} displacement.⁶¹ Nevertheless, we summarize this anomalous behavior of Raman spectral modes with temperature to have a multitude of possible reasons and derivations, other than the concepts of local structure deformation or a new spin reorientation. To ascertain the exact origin of the anomaly requires a detailed and simultaneous study of the structural and magnetic aspects of BFO.

To study the optical properties of BFO thin films, transmission spectra and diffuse reflection spectra are obtained. The optical spectra of BFO-A thin films show 53% to 80% transmission in the energy range of 2 eV to 0.7 eV [Fig. 5(a)], whereas, the transmission is found to be 40% to 64% for BFO-V and show a decrease in the transmission of $\sim 20\%$ at 0.7 eV. Both BFO-A and BFO-V thin films exhibit a sharp decrease in transmission due to the band edge absorption in the visible light region. This is also inferred from the sharp change in the % of reflection in diffuse reflection spectra. The optical bandgap is estimated from the Tauc plot using the Kubelka-Munk (K-M) function [Fig. 5(b)], $F(R)$, given by $F(R) = \frac{(1-R)^2}{2R}$, where R is the diffuse reflectance of the material. $(\alpha h\nu)^2 = (h\nu - E_g)$ with $\alpha = F(R)$ being plotted against $h\nu$ for direct bandgap semiconductors as shown in Fig. 5(b). Bandgap values (E_g) are obtained from the intersection of a straight line drawn from the absorption edge region and extrapolating this band edge line to the abscissa in the Tauc plot. The main absorption edge in the range of 2.0 to 2.5 eV corresponds to the charge

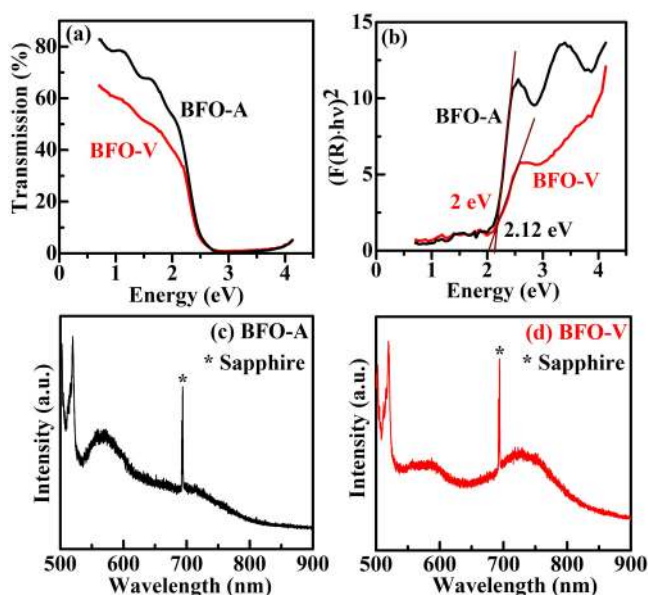


FIG. 5. (a) Transmission spectra and (b) Tauc plot using the Kubelka-Munk function of BFO-A and BFO-V thin films. Photoluminescence spectra of (c) BFO-A and (d) BFO-V films using an excitation wavelength of 488 nm. *The sharp emission in (c) and (d) arise from the sapphire substrate.

transfer between O $2p$ to Fe $3d$. Bandgap values calculated from Tauc plots are found to be 2.12 eV and 2 eV for BFO-A and BFO-V thin films. Due to the vacuum annealing process, the optical bandgap is found to decrease slightly for BFO thin films. The oxygen vacancies are shown to decrease the bandgap significantly due to oxygen defect induced microstrain and under coordinated oxygen on the surface of nanoparticles.⁶²

In our previous studies, we have established that the defect levels formed due to oxygen vacancies (O_V) are located between conduction and valence bands.^{63,64} The oxygen vacancy related defect states created by surface dangling bonds, surface defects, and interior defects are shown to lie with closer energy levels within the pristine BiFeO_3 bandgap.^{63,64} These states reduce the optical bandgap of the material and provide a diffused transition (BFO-V) rather than giving a sharp band-to-band transition (BFO-A) [Fig. 5(b)]. The presence of such energy levels leads to broad transition near the band edge in the absorption spectra. Few other absorption edges are observed in BFO-A thin films in the range of 3 eV to 4 eV. These are attributed to the charge transfer transition in the $d-d$ energy levels of the transition metal, i.e., Fe (1) $3d$ to Fe (2) $3d$.⁶⁵ Vacuum annealing also shows a decrease in transmission (%) in BFO-V films in the visible-NIR region by about 20% compared to that observed in BFO-A films. The reduction in transmission (%) in the vis-NIR region could be attributed to an enhanced $d-d$ absorption and defect-related absorption characteristics in the NIR region.

The dependence of transmission of a film on oxygen vacancies (O_V), surface roughness, and impurity centers as other possibility

has been discussed by Gaur *et al.*⁶⁶ Scattering can be enhanced from the film surface due to surface roughness and cracks present at the film surface.^{66,67} However, examining the samples by SEM confirmed that there are no cracks in our samples. AFM studies (discussed in the following text) also showed no drastic changes in the roughness. The reduction of transmission has also been attributed to increased light scattering from grain boundaries with the reduction of grain size.⁶⁷ Since the particle size has not changed drastically even after subjecting to different annealing conditions, the change in transmission is not expected to get affected. It is clear from both SEM and AFM topography images that BFO-A and BFO-V films have almost similar surface morphology and roughness. Scattering from the surfaces of both the films is also similar. Doping or defects created within the lattice will create lattice distortion and stress resulting in changed optical properties of the thin films.⁶⁸ Therefore, we believe that this change is associated with the defects originating from O_V in BFO-V films due to vacuum annealing.

The effect of vacuum annealing is also seen in the photoluminescence (PL) spectra obtained using 488 nm laser excitation shown in Fig. 5. PL spectra obtained using a 488 nm excitation (blue line from Ar ion laser) in a Raman spectrometer (Horiba Jobin-Yvon (HR800 UV)) for BFO-A and BFO-V films are shown in Figs. 5(c) and 5(d), respectively. A narrow intense doublet peak noticed at 692.5 nm and 694 nm in both BFO-A and BFO-V films is due to the (0001) oriented sapphire substrate.⁶⁹ A sharp peak observed at 520 nm in both the films is a two-phonon Raman spectral feature. BFO-A films show a broad peak at a wavelength of 570 nm ($E_g \sim 2.18$ eV), which corresponds to a band-to-band transition. In addition to this peak, another broader peak is observed at 715 nm, which could be attributed to the transition from the intermediate band energy levels located between the conduction and valence bands. Such intermediate bands are known to arise from defects mostly due to oxygen vacancies. In the case of BFO-V films, initial broad peak due to band edge transition shows a slight decrease to 586 nm ($E_g \sim 2.12$ eV). This observation is consistent with that made from the Tauc plot [Fig. 5(b)] analysis. Interestingly, the broad peak seen at 730 nm increases in intensity in BFO-V indicating the vacuum annealing would result in increased oxygen vacancy concentration and thus enhancing the defect density energy state in the interband region.

We measured the dielectric constant of BFO-A and BFO-V films at room temperature in the frequency range of 100 kHz to 10 MHz. Two contacts, each of 0.09 cm^2 area ($\sim 3 \times 3 \text{ mm}^2$) made on the top side of thin films with 1 mm separation were used as electrodes. Variation of dielectric constant with frequency is shown in Fig. S4 (supplementary material). It is found that the dielectric constant of BFO-A and BFO-V films varies in the range of 80 to 65 for the former and 60 to 55 for the latter. A slight decrease in the dielectric constant for the BFO-V can be attributed to the vacuum annealing process, in which the conductivity of the film becomes better. The values are 70 and 56, respectively, at 1 MHz frequency and are comparable to the reported values.^{70–72}

A good estimation of the quality of the thin films grown by the CSD process can be discerned from the ferroelectric nature of thin films. We carried out piezoforce microscope (PFM) images on BFO-A and BFO-V thin films to get the ferroelectric domain details. Figures 6(a)–6(c) and 6(e)–6(g) show the topography,

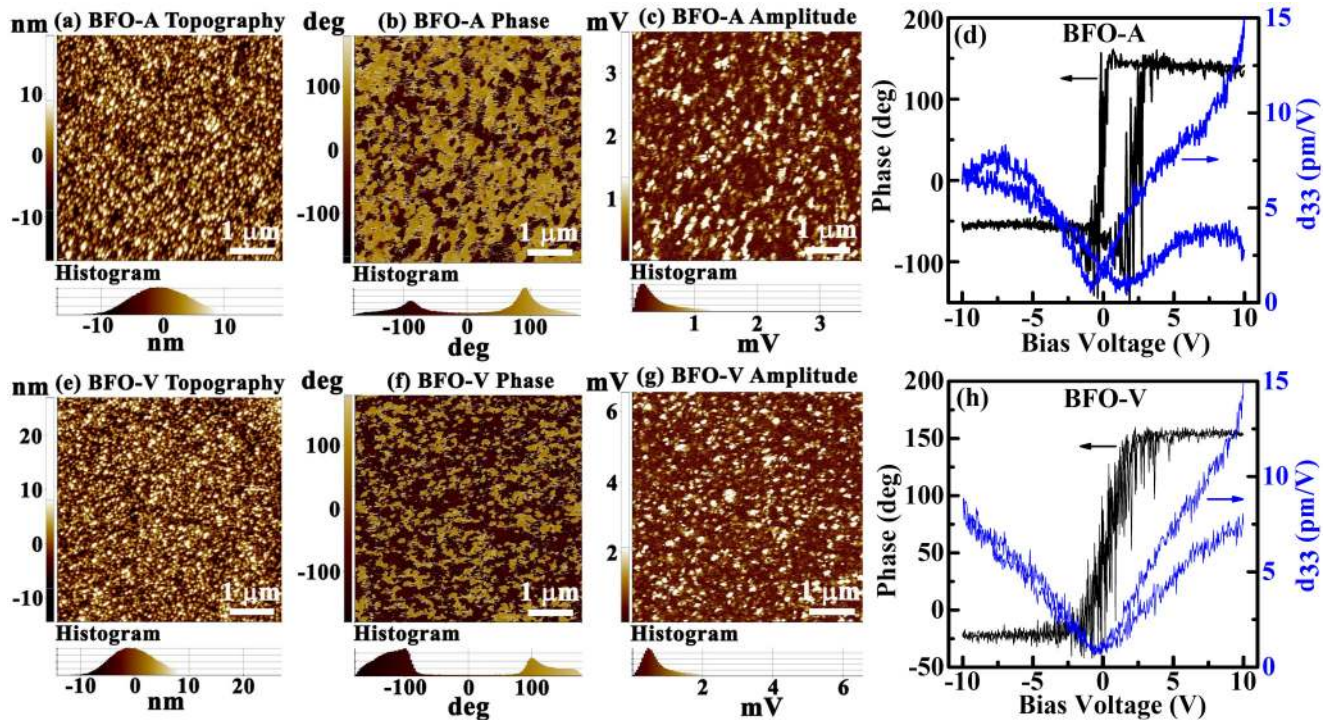


FIG. 6. Piezoelectric force microscopy images of (a) and (e) topography, (b) and (f) phase, and (c) and (g) amplitude of (a)–(c) BFO-A and (e)–(g) BFO-V films, respectively, on the sapphire substrate. (d) and (h) Piezoelectric phase switching and piezoelectric coefficient (d_{33}) measured at a given point in (d) BFO-A and (h) BFO-V thin films.

phase, and amplitude mapping in a scan area of $5 \times 5 \mu\text{m}^2$ of BFO-A and BFO-V thin films, respectively. PFM topography images of BFO-A and BFO-V show an average roughness of ~ 4 nm. The grain sizes are in the range of $110 \text{ nm} \pm 15 \text{ nm}$, which are consistent with the grain size estimated from FESEM images. The morphology of vacuum annealed films remains the same as that of air-annealed films. PFM out-of-plane phase image confirms the presence of ferroelectric domains. Sharp color contrast is seen from the domains oriented with a 180° phase difference. Many adjacent particles share the same polarization as discerned from the domain orientation, thus the domains are much larger than the particle size. Both BFO-A and BFO-V show similar PFM images suggesting that the oxygen vacancies created due to the vacuum annealing process do not drastically affect the ferroelectric nature of the particles. Few hundred-nanometer size of ferroelectric domains found in the PFM phase image further suggests high quality of BFO thin films. Since the films are made on sapphire substrates, we could not do the P-E loop or current loop measurements, therefore obtained piezoelectric switching and piezoelectric coefficient (d_{33}) measurements to validate the true ferroelectric nature of the thin films. Ag contacts were made on the surface of films to apply bias and measure polarization phase switching and piezoelectric measurements in these films.

The piezoelectric switching and piezoelectric coefficient (d_{33}) measurements acquired by the PFM technique on BFO-A and

BFO-V films are given in Figs. 6(d) and 6(h). Both the films show the polarization switching with a phase change of 180° when measured in the nanoscale region under the voltage sweep from -10 V to $+10$ V. The BFO-A film exhibits a clear hysteretic open square loop showing the ferroelectric domain switching. But, BFO-V films showed a S shape curve without hysteresis. This behavior is checked by repeating the measurements at different places on the films and representative characteristic curves are given in Fig. 6. The values of piezoelectric coefficient d_{33} calculated from amplitude (5 to 10 pm/V), shown in the same plot, are characteristics of BiFeO_3 structure. d_{33} value observed in BFO thin films is around 5–10 pm/V, which is slightly low compared to other epitaxial films. For example, Gonzalez *et al.*⁷³ have shown a high d_{33} value of 40 pm/V for $(100)_{\text{pc}}$ oriented BiFeO_3 thin films (thickness ~ 300 nm) coated on Pt (111)/Ti/SiO₂/Si substrates. Such low values in our films could be because of slight dispersion in the $(100)_{\text{pc}}$ orientation and the polarization not being exactly perpendicular to the film due to the in-plane biasing. In our study, clear hysteresis seen in the plot is the signature of the quality of the oriented films grown. Both the films show the piezoelectric response. The piezoelectric loop also exhibits the same trend as the phase loop observed in these films. The change in the ferroelectric hysteresis characteristics in the vacuum annealed thin films is due to the O_V created in the films. It has been reported that O_V suppresses the ferroelectric nature of BiFeO_3 .^{74,75}

In BFO-V films, the ferroelectric property is not completely suppressed. However, it shows hysteresis with no coercivity.

Magnetic properties of (100)_{pc} oriented BFO-A and BFO-V thin films were measured using a VSM SQUID magnetometer. M vs H plots measured at 5 K and 300 K with the field applied parallel [in-plane (IP)] and perpendicular [out-of-plane (OP)] to the substrate surface of BFO-A/sapphire(0001) and BFO-V/sapphire(0001) thin films are shown in Fig. 7. M-H measurements were performed with a maximum applied magnetic field of 7 T. The acquired data have a large diamagnetic contribution from the sapphire substrate [Figs. 7(a)–7(d)]. The linear variation of M with the applied magnetic field for $H > 20$ kOe in the M-H plot (i.e., negative slope) arising from the diamagnetic contribution of sapphire substrate is subtracted and the corrected M vs H plots are given in Figs. 8(a) and 8(b) for BFO-A and Figs. 8(d) and 8(e) for BFO-V. Saturation magnetization (M_S), remanent magnetization (M_R), and coercive field (H_C) values for IP and OP measurements at 5 K and 300 K for both BFO-A and BFO-V films are listed in Table I. It is observed that in-plane saturation magnetization M_S is three to four times higher than out-of-plane M_S for BFO-A at 5 K. Furthermore, the coercive field is three to four times higher when M-H plots are measured in OP ($H_C = 4.4$ kOe) than IP ($H_C = 1.3$ kOe) at 5 K. This suggests a strong anisotropy present in the system with the magnetic moments preferably oriented along the film surface.

While similar anisotropy is observed at 300 K, the difference in the saturation magnetization between the IP and OP measurement is small with the former 25% more than the latter. A small difference in H_C is found for IP and OP measurements at 300 K (Table I). We find almost three and five times enhancement in M_S values, both in IP and OP M-H measurements at 5 K and 300 K, for BFO-V compared to BFO-A thin films. Five times increment in

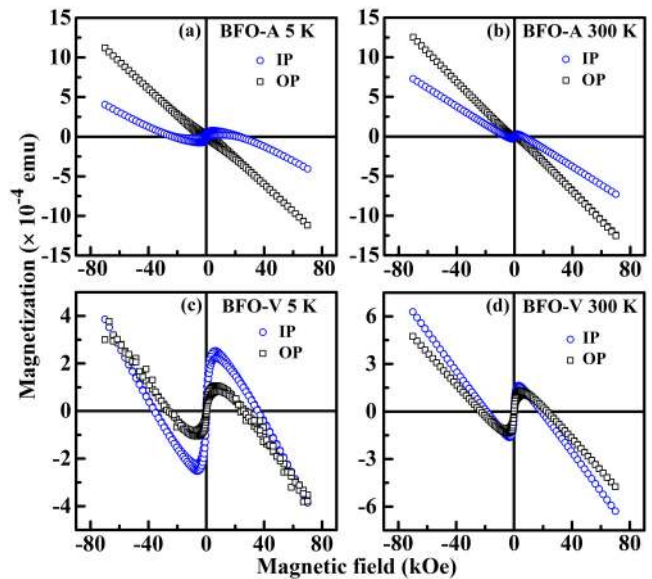


FIG. 7. As-measured magnetization vs magnetic field (M vs H) curves with field applied parallel to out-of-plane (OP) and in-plane (IP) of the substrate for (a) and (b) BFO-A, and (c) and (d) BFO-V thin films coated on sapphire. (a) and (c) are measured at 5 K and (b) and (d) are measured at 300 K.

M_S is also noticed at room temperature (300 K) in both IP and OP conditions. The enhancement of M_S in BFO-V films could be due to the perturbation in spin cycloid present in BFO-A films by oxygen vacancies created during the vacuum annealing process.⁶⁰

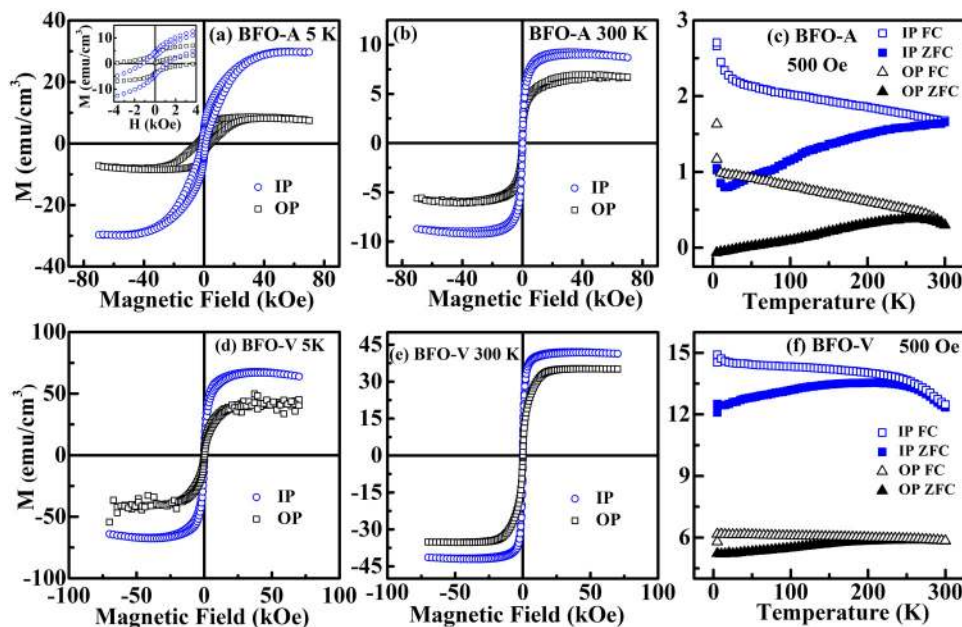


FIG. 8. Magnetization vs magnetic field (M vs H) curves after subtracting the diamagnetic contribution of the curves given in Fig. 7 for (a) and (b) BFO-A and (d) and (e) BFO-V thin films on sapphire. M vs H curves with field applied parallel to out-of-plane (OP) and in-plane (IP) of the substrate are given. (a) and (d) are measured at 5 K, and (b) and (e) are measured at 300 K. The inset in (a) shows the magnified portion of M vs H curve given in the main panel. Low temperature ZFC-FC curves for (c) BFO-A and (f) BFO-V measured in the temperature range of 5 K to 300 K under a constant magnetic field of 500 Oe applied both in OP and IP.

TABLE I. Saturation magnetization (M_S), remanent magnetization (M_R), and coercive field (H_C) values for in-plane (IP) and out-of-plane (OP) configurations at 5 K and 300 K for both BFO-A and BFO-V thin films.

Sample	Temperature (K)	Configuration	M_S (emu/cm ³)	M_R (emu/cm ³)	H_C (kOe)
BFO-A	5	IP	29.8	4.7	1.3
		OP	8.2	3.9	4.4
	300	IP	9.2	0.8	0.12
		OP	6.9	0.5	0.15
BFO-V	5	IP	67.6	5.1	0.15
		OP	41.2	3.3	0.24
	300	IP	41.7	0.5	0.01
		OP	35.2	0.4	0.01

Oxygen vacancies affect Fe–O–Fe bond angle, which breaks antiferromagnetic coupling between two Fe ions and distort the FeO₆ octahedra. It has been demonstrated in the BiFeO₃ system that O_V play a significant role in altering the Fe–O–Fe bond angles as discerned from the XANES studies.⁶⁵ We surmise similar effect causes the changes in the magnetic properties in BiFeO₃. The uncompensated magnetic moments strongly interact leading to the enhanced magnetization as discussed below. The change in Fe–O bond is also ascertained by observing the two-phonon modes obtained from Raman spectroscopy for BFO-A and BFO-V films (see Fig. S5 in the [supplementary material](#)).

Magnetic anisotropy of BFO-V films, similar to BFO-A film, is also evident from M-H plots. In-plane M_S is 1.6 and 1.2 times higher than out-of-plane M_S at 5 K and 300 K, respectively, in BFO-V film. M_R [5.1 emu/cm³ (IP) and 3.3 emu/cm³ (OP) at 5 K; 0.5 emu/cm³ (IP) and 0.4 emu/cm³ (OP) at 300 K] and H_C [150 Oe (IP) and 240 Oe (OP) at 5 K; 10 Oe (IP) and 12 Oe (OP) at 300 K] for BFO-V are found to be very small in both IP and OP conditions suggesting severe softening of magnetization in BFO-V thin films ([Table I](#)). In-plane M_S observed in BFO-V films at room temperature (300 K) is 41.7 emu/cm³, which is almost similar to the observations made by Zhang *et al.* for polycrystalline BiFeO₃ thin films grown on Si substrates using the spin coating technique.⁷⁶ Saturation magnetization of 40 emu/cm³ is reported at room temperature. Most of the reported values of magnetization, specifically on the nanoparticulate thin films, range from 0.65 emu/cm³ (0.08 emu/g) to 180 emu/cm³ (21.58 emu/g). The highest value of magnetization of ~22 emu/g has been reported in the phase pure BiFeO₃ system.^{4,76–84} The observed in-plane M_S values for BFO-V films are 41.7 emu/cm³ (5 emu/g) at 300 K and 67.6 emu/cm³ (8.1 emu/g) at 5 K. The vacuum annealed films exhibit higher magnetization than BFO-A films [The magnetization values for the BFO-A thin films are 9.2 emu/cm³ (1.1 emu/g) at 300 K and 29.8 emu/cm³ (3.6 emu/g) at 5 K]. The large values of magnetization can be understood from the breaking of spin cycloid, either by the introduction of oxygen vacancies or by the size reduction. The former gives rise to large magnetization than the latter.^{60,85} In our previous study, we have shown a systematic change in the magnetization influenced by the O_V introduced in the lattice as well

controlled by the size of the particles. Since the size of the particles does not get altered due to the annealing process, we attribute the O_V influence the magnetic properties significantly in BiFeO₃ thin films. Although many literature reports have suggested nondecipherable magnetic phases could contribute to the magnetization, we contemplate that such impurities have hardly any contribution to the magnetization in our films.

[Figures 8\(c\)](#) and [8\(f\)](#) show field dependent zero-field-cooled (ZFC)—field-cooled (FC) curves of BFO-A and BFO-V thin films, respectively, under an applied magnetic field of 500 Oe. The BFO-A thin film shows a linear dependence on magnetization with temperature which confirms the absence of magnetic defects or superparamagnetic feature.⁸⁶ Splitting observed in ZFC-FC curves for BFO-A is attributed to the presence of both antiferromagnetic and ferromagnetic components in the film.⁸⁷ Magnetization increases sharply below 30 K indicating the presence of some paramagnetic species, mostly Fe³⁺, on the surface of crystallites.⁶⁰ On the other hand, the effect of the surface disorder paramagnetic component is minimal in the OP configuration. Splitting between ZFC-FC curves till room temperature suggests that both films may exhibit ferromagnetic transition temperature well above room temperature. The splitting between ZFC-FC curves is reduced in BFO-V films in both IP and OP configurations. The temperature at which overlapping of ZFC-FC data observed in the case of OP (~175 K) is shifted toward lower temperature compared to the IP configuration (~250 K) of BFO-V films, which confirms the anisotropy of spin orientation unequivocally in vacuum annealed films. This effect is minimal in BFO-A films due to the low magnetization value at magnetic field of 500 Oe.

We investigated the photoconductivity response of BFO-A and BFO-V thin films [shown in [Figs. 9\(a\)](#) and [9\(b\)](#)]. The BFO-A film shows an initial conductivity of 8.75×10^{-11} S/cm in dark conditions. The conductivity is found to increase during light ON condition and saturates within 5 min. The change in the conductivity on AM1.5 one Sun illumination is found to be $\sim 5 \times 10^{-12}$ S/cm for BFO-A. The conductivity decreases and reaches lower values than the initial conductivity when the illumination is turned OFF. All the four cycles represent the same behavior and conductivity keeps decreasing with the number of cycles. In contrast, the BFO-V film shows an initial conductivity of 3×10^{-10} S/cm which is one order higher than the initial conductivity of BFO-A. The increase in the conductivity in BFO-V films is due to oxygen vacancies created during the time of vacuum annealing. The conductivity increase in BFO-V films is 4×10^{-11} S/cm during light ON for 5 min. The conductivity of BFO-V thin films also shows a decrease when the illumination is turned OFF. Time dependent conductivity changes, both increasing and decreasing segments of the conductivity curves, are fitted with exponential equations to understand the relaxation behavior of carrier generation and recombination. [Figures 9\(c\)](#) and [9\(d\)](#) show the fitted curves with the original data. By fitting the rising part of the conductivity using the exponential equation $\frac{\sigma_t - \sigma_{\text{off}}}{\sigma_{\text{on}} - \sigma_{\text{off}}} = \frac{\Delta\sigma_t}{\Delta\sigma_{\text{total}}} = a \left(1 - e^{-\frac{t}{\tau_g}}\right)$, where $\Delta\sigma_t$ ($= \sigma_t - \sigma_{\text{off}}$) is the difference in conductivity at time t (σ_t) with respect to OFF condition (σ_{off}), $\Delta\sigma_{\text{total}}$ ($= \sigma_{\text{on}} - \sigma_{\text{off}}$) is the difference in conductivity between ON (σ_{on}) and OFF (σ_{off}) states and a is a constant, average carrier generation lifetimes (τ_g) are found.^{63,64} Carrier generation

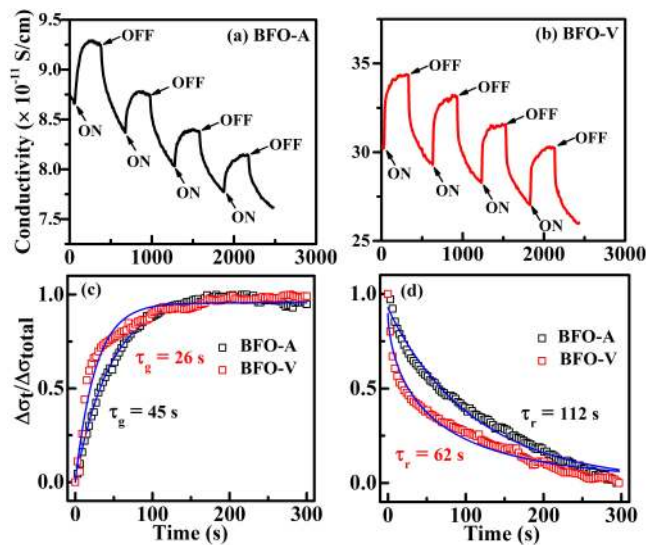


FIG. 9. Photoconductivity response of (a) BFO-A and (b) BFO-V thin films under the ON and OFF states of AM1.5 filtered 1 Sun illumination source. (c) and (d) show the increasing and decreasing segments of photoconductivity response under the ON and OFF states of solar simulator source, respectively. The open symbols show the measured response, and the solid line is the exponential fit.

lifetimes are found to be 45 s and 26 s in BFO-A and BFO-V, respectively. The decreasing part of conductivity is fitted using the stretched exponential function $\frac{\sigma_i - \sigma_{off}}{\sigma_{on} - \sigma_{off}} = \frac{\Delta\sigma_i}{\Delta\sigma_{total}} = a e^{-\left(\frac{t}{\tau_r}\right)^b}$, where τ_r is the carrier recombination lifetime, a is a constant, and b indicates the deviation from the exponential function. Carrier recombination lifetimes are found to be 112 s and 62 s in BFO-A and BFO-V, respectively. It is noticed from the exponential fitting that both generation (τ_g) and recombination (τ_r) are faster in BFO-V films than in BFO-A.

Carrier generation and recombination are known to generally take place by the direct band-to-band transition. Such transitions are much faster ($<1 \mu\text{s}$) than the values reported in this manuscript. But in the present study, carrier generation and recombination lifetimes are longer due to the involvement of shallow and deep defect states present between valence and conduction bands.⁸⁸ While, electrons in the valence band absorb light, with a photon energy greater than the bandgap energy, to get excited to the conduction band, photons with a wide range of wavelength can get absorbed due to the shallow defect levels present within the bandgap region. Further, deep defect levels formed due to ionic vacancies in bulk can act as charge trap states for photogenerated charge carriers. The electrons trapped in the deep defect states lead the longer generation and recombination time. This mechanism of carrier generation and recombination is explained in our previous reports revealing the role of oxygen vacancies on the photoconductivity in BiFeO₃ nanoparticle ceramics.^{63,64} The photoconductivity studies carried out on glass/FTO/BFO and Si/SiO₂/BFO using coplanar in-plane electrical contacts also show large photoconductivity

compared to the sapphire/BFO films (see Figs. S6 and S7 of the [supplementary material](#)). The leakage current from the BFO films grown on the sapphire substrate is very small (Fig. S8). We surmise that the anisotropic conducting property might play a significant role for such observations. These studies, thus, suggest that highly oriented BiFeO₃ thin films with tailored physical properties will be of significant use for ferroelectric, magnetoelectric, and photovoltaic applications.

IV. CONCLUSION

In conclusion, (100)_{pc} oriented BiFeO₃ thin films are grown on the sapphire (0001) substrate using the simple chemical solution deposition technique by the one step spin coating method. The effect of vacuum annealing on the structural, optical, ferroelectric, magnetic, and photoconductivity properties is investigated. A bandgap reduction is observed due to the vacuum annealing of BiFeO₃ thin films due to the formation of defect states in between valence and conduction bands. Temperature-dependent Raman spectral studies exhibit sharp transitions confirming the high quality of thin films. O_V in BiFeO₃ blue shifts the A₁(TO) and E (TO) modes due to the perturbation in Bi–O bonds. Ferroelectric domain sizes are found to be larger than the grain sizes and the domains are unaltered despite vacuum annealing treatment. A reduction in ferroelectric hysteresis switching in BFO-V signifies the decrement in the ferroelectric property due to the presence of O_V. An enhancement in magnetic and photoconductivity properties is observed in vacuum annealed thin films. While the magnetization is shown to increase by three to five times, one order increase in photoconductivity is evidenced in vacuum annealed thin films. O_V affects Fe–O–Fe bond characteristics and distorts the FeO₆ octahedra, resulting in the breaking of antiferromagnetic coupling between two Fe ions. The uncompensated magnetic moments strongly interact leading to the enhanced magnetization. Air-annealed BFO thin films have strong anisotropy with the easy magnetization along the substrate surface. The anisotropy, though found in vacuum annealed BFO thin films, has mellowed down due to O_V. In stark contrast, hard magnetic characteristics of air-annealed BiFeO₃ thin films turning into soft magnetic material on vacuum annealing is also evidenced. The influence and importance of O_V on different physical properties are demonstrated.

This study provides a detailed insight into tailoring the optical, electrical, magnetic, and photoconductivity properties of highly oriented BiFeO₃ thin films grown by the facile chemical solution deposition method, which will be useful under optimized growth and processing conditions for a multitude of applications including magnetoelectrics, photoferroelectrics, and photodetectors.

SUPPLEMENTARY MATERIAL

See the [supplementary material](#) for XRD and SEM of 3 h annealed samples, XRD data of polycrystalline films grown on different substrates, dielectric constant vs frequency plot, deconvoluted two-phonon modes, table summarizing various anomalies observed in temperature-dependent Raman spectra, photoconductivity responses using coplanar in-plane and interdigitated contacts, and the dc I-V plots.

ACKNOWLEDGMENTS

C.S. acknowledges the support from DST-SERB through Grant No. EMR/2016/002785 and the support from DST-SERI through Grant No. DST/TM/SERI/2K11/113.

REFERENCES

- ¹K. F. Wang, J.-M. Liu, and Z. F. Ren, *Adv. Phys.* **58**(4), 321–448 (2009).
- ²Y. H. Chu, Q. Zhan, C.-H. Yang, M. P. Cruz, L. W. Martin, T. Zhao, P. Yu, R. Ramesh, P. T. Joseph, I. N. Lin, W. Tian, and D. G. Schlom, *Appl. Phys. Lett.* **92**(10), 102909 (2008).
- ³G. Catalan and J. F. Scott, *Adv. Mater.* **21**(24), 2463–2485 (2009).
- ⁴J. Wang, J. B. Neaton, H. Zheng, V. Nagarajan, S. B. Ogale, B. Liu, D. Viehland, V. Vaithyanathan, D. G. Schlom, U. V. Waghmare, N. A. Spaldin, K. M. Rabe, M. Wuttig, and R. Ramesh, *Science* **299**(5613), 1719–1722 (2003).
- ⁵K. Yin, M. Li, Y. Liu, C. He, F. Zhuge, B. Chen, W. Lu, X. Pan, and R.-W. Li, *Appl. Phys. Lett.* **97**(4), 042101 (2010).
- ⁶R. K. Katiyar, Y. Sharma, D. G. B. Diestra, P. Misra, S. Kooriyattil, S. P. Pavunny, G. Morell, B. R. Weiner, J. F. Scott, and R. S. Katiyar, *AIP Adv.* **5**(3), 037109 (2015).
- ⁷T. Choi, S. Lee, Y. J. Choi, V. Kiryukhin, and S.-W. Cheong, *Science* **324**(5923), 63–66 (2009).
- ⁸H.-M. Xu, H.-C. Wang, Y. Shen, Y.-H. Lin, and C.-W. Nan, *J. Appl. Phys.* **116**(17), 174307 (2014).
- ⁹S. Li, Y.-H. Lin, B.-P. Zhang, Y. Wang, and C.-W. Nan, *J. Phys. Chem. C* **114**(7), 2903–2908 (2010).
- ¹⁰Y. Lin, G. Yuan, R. Liu, S. Zhou, S. W. Sheehan, and D. Wang, *Chem. Phys. Lett.* **507**(4), 209–215 (2011).
- ¹¹J. Wu, Z. Fan, D. Xiao, J. Zhu, and J. Wang, *Prog. Mater. Sci.* **84**, 335–402 (2016).
- ¹²Z. Chen, L. He, F. Zhang, J. Jiang, J. Meng, B. Zhao, and A. Jiang, *J. Appl. Phys.* **113**(18), 184106 (2013).
- ¹³Ch. Binek and B. Doudin, *J. Phys. Condens. Matter* **17**(2), L39 (2005).
- ¹⁴R. Agarwal, Y. Sharma, and R. S. Katiyar, *Appl. Phys. Lett.* **107**(16), 162904 (2015).
- ¹⁵R. K. Katiyar, Y. Sharma, P. Misra, V. S. Puli, S. Sahoo, A. Kumar, J. F. Scott, G. Morell, B. R. Weiner, and R. S. Katiyar, *Appl. Phys. Lett.* **105**(17), 172904 (2014).
- ¹⁶R. Guo, L. You, Y. Zhou, Z. Shih Lim, X. Zou, L. Chen, R. Ramesh, and J. Wang, *Nat. Commun.* **4**, 1990 (2013).
- ¹⁷D. Sando, A. Barthélémy, and M. Bibes, *J. Phys. Condens. Matter* **26**(47), 473201 (2014).
- ¹⁸A. Bhatnagar, Y. H. Kim, D. Hesse, and M. Alexe, *Nano Lett.* **14**(9), 5224–5228 (2014).
- ¹⁹I.-T. Bae, T. Ichinose, M.-G. Han, Y. Zhu, S. Yasui, and H. Naganuma, *Sci. Rep.* **8**(1), 893 (2018).
- ²⁰J. Wang, H. Zheng, Z. Ma, S. Prasertchoung, M. Wuttig, R. Droopad, J. Yu, K. Eisenbeiser, and R. Ramesh, *Appl. Phys. Lett.* **85**(13), 2574–2576 (2004).
- ²¹Y.-H. Lee, J.-M. Wu, Y.-L. Chueh, and L.-J. Chou, *Appl. Phys. Lett.* **87**(17), 172901 (2005).
- ²²R. Y. Zheng, X. S. Gao, Z. H. Zhou, and J. Wang, *J. Appl. Phys.* **101**(5), 054104 (2007).
- ²³J. F. Ihlefeld, A. Kumar, V. Gopalan, D. G. Schlom, Y. B. Chen, X. Q. Pan, T. Heeg, J. Schubert, X. Ke, P. Schiffer, J. Orenstein, L. W. Martin, Y. H. Chu, and R. Ramesh, *Appl. Phys. Lett.* **91**(7), 071922 (2007).
- ²⁴J. F. Ihlefeld, N. J. Podraza, Z. K. Liu, R. C. Rai, X. Xu, T. Heeg, Y. B. Chen, J. Li, R. W. Collins, J. L. Musfeldt, X. Q. Pan, J. Schubert, R. Ramesh, and D. G. Schlom, *Appl. Phys. Lett.* **92**(14), 142908 (2008).
- ²⁵S. Y. Yang, F. Zavaliche, L. Mohaddes-Ardabili, V. Vaithyanathan, D. G. Schlom, Y. J. Lee, Y. H. Chu, M. P. Cruz, Q. Zhan, T. Zhao, and R. Ramesh, *Appl. Phys. Lett.* **87**(10), 102903 (2005).
- ²⁶M. S. Kartavtseva, O. Y. Gorbenko, A. R. Kaul, and S. A. Savinov, *J. Surf. Invest. X-ray Synchrotr. Neutron Tech.* **2**(1), 1–11 (2008).
- ²⁷T. Hosokura, A. Ando, and T. Konoike, *RSC Adv.* **5**(118), 97563–97567 (2015).
- ²⁸H. G. Yeo and S. Trolrier-McKinstry, *J. Appl. Phys.* **116**(1), 014105 (2014).
- ²⁹F. M. Pontes, E. Longo, E. R. Leite, E. J. H. Lee, J. A. Varela, P. S. Pizani, C. E. M. Campos, F. Lanciotti, V. Mastellaro, and C. D. Pinheiro, *Mater. Chem. Phys.* **77**(2), 598–602 (2003).
- ³⁰H. Naganuma and S. Okamura, *J. Appl. Phys.* **101**(9), 09M103 (2007).
- ³¹S. K. Singh, H. Ishiwara, and K. Maruyama, *J. Appl. Phys.* **100**(6), 064102 (2006).
- ³²P. K. Siwach, H. K. Singh, J. Singh, and O. N. Srivastava, *Appl. Phys. Lett.* **91**(12), 122503 (2007).
- ³³S. K. Singh, Y. K. Kim, H. Funakubo, and H. Ishiwara, *Appl. Phys. Lett.* **88**(16), 162904 (2006).
- ³⁴F. Tyholdt, H. Fjellvåg, A. E. Gunnæs, and A. Olsen, *J. Appl. Phys.* **102**(7), 074108 (2007).
- ³⁵F. Tyholdt, S. Jørgensen, H. Fjellvåg, and A. E. Gunnæs, *J. Mater. Res.* **20**(8), 2127–2139 (2005).
- ³⁶Q. Zhang, N. Valanoor, and O. Standard, *J. Appl. Phys.* **116**(6), 066810 (2014).
- ³⁷Y. Zhou, L. Fang, L. You, P. Ren, L. Wang, and J. Wang, *Appl. Phys. Lett.* **105**(25), 252903 (2014).
- ³⁸J. Xing, E.-J. Guo, J. Dong, H. Hao, Z. Zheng, and C. Zhao, *Appl. Phys. Lett.* **106**(3), 033504 (2015).
- ³⁹S. Y. Yang, J. Seidel, S. J. Byrnes, P. Shafer, C.-H. Yang, M. D. Rossell, P. Yu, Y.-H. Chu, J. F. Scott, J. W. Ager III, L. W. Martin, and R. Ramesh, *Nat. Nanotechnol.* **5**, 143 (2010).
- ⁴⁰S. J. A. Moniz, R. Quesada-Cabrera, C. S. Blackman, J. Tang, P. Southern, P. M. Weaver, and C. J. Carmalt, *J. Mater. Chem. A* **2**(9), 2922–2927 (2014).
- ⁴¹K. Min, F. Huang, Y. Jin, X. Lu, H. Wu, and J. Zhu, *J. Phys. D Appl. Phys.* **48**(44), 445301 (2015).
- ⁴²S. Guillin, S. Jian, N. Zhang, and C. Fanggao, *Phys. B Condens. Matter* **493**, 47–52 (2016).
- ⁴³T. Wang, S.-H. Song, M. Wang, J.-Q. Li, and M. Ravi, *Ceram. Int.* **42**(6), 7328–7335 (2016).
- ⁴⁴P. Kharel, S. Talebi, B. Ramachandran, A. Dixit, V. M. Naik, M. B. Sahana, C. Sudakar, R. Naik, M. S. R. Rao, and G. Lawes, *J. Phys. Condens. Matter* **21**(3), 036001 (2009).
- ⁴⁵H. Liu, R. Liu, and T. Liu, *J. Sol Gel Sci. Technol.* **57**(1), 1–5 (2011).
- ⁴⁶X. Qi, J. Dho, M. Blamire, Q. Jia, J.-S. Lee, S. Foltyn, and J. L. MacManus-Driscoll, *J. Magn. Magn. Mater.* **283**(2), 415–421 (2004).
- ⁴⁷R. Palai, H. Schmid, J. F. Scott, and R. S. Katiyar, *Phys. Rev. B* **81**(6), 064110 (2010).
- ⁴⁸P. S. V. Mocherla, C. Karthik, R. Ubic, M. S. R. Rao, and C. Sudakar, *Appl. Phys. Lett.* **105**(13), 132409 (2014).
- ⁴⁹J. Gebhardt and A. M. Rappe, *Phys. Rev. B* **98**(12), 125202 (2018).
- ⁵⁰M. R. Catalano, G. Spedalotto, G. G. Condorelli, and G. Malandrino, *Adv. Mater. Interfaces* **4**(8), 1601025 (2017).
- ⁵¹S. Hussain, F. A. Khan, M. Aftab, M. Waseem, and S. U. Awan, *J. Electron. Mater.* **48**(7), 4273 (2019).
- ⁵²R. Palai, R. S. Katiyar, H. Schmid, P. Tissot, S. J. Clark, J. Robertson, S. A. T. Redfern, G. Catalan, and J. F. Scott, *Phys. Rev. B* **77**(1), 014110 (2008).
- ⁵³R. Haumont, J. Kreisel, and P. Bouvier, *Phase Transit.* **79**(12), 1043–1064 (2006).
- ⁵⁴A. Ahlawat, S. Satapathy, S. Maan, V. G. Sathe, and P. K. Gupta, *J. Raman Spectrosc.* **45**(10), 958–962 (2014).
- ⁵⁵D. Rout, K.-S. Moon, and S.-J. L. Kang, *J. Raman Spectrosc.* **40**(6), 618–626 (2009).
- ⁵⁶K. S. Manoj, S. K. Ram, and J. F. Scott, *J. Phys. Condens. Matter* **20**(25), 252203 (2008).
- ⁵⁷A. Kumar, N. M. Murari, and R. S. Katiyar, *Appl. Phys. Lett.* **92**(15), 152907 (2008).

- ⁵⁸Z. Duan, Q. Yu, J. Wu, J. Sun, Z. Hu, and J. Chu, *Thin Solid Films* **525**, 188–194 (2012).
- ⁵⁹A. Jaiswal, R. Das, T. Maity, K. Vivekanand, S. Adyanthaya, and P. Poddar, *J. Phys. Chem. C* **114**(29), 12432–12439 (2010).
- ⁶⁰S. V. M. Pavana, M. B. Sahana, R. Gopalan, M. S. R. Rao, B. R. K. Nanda, and C. Sudakar, *Mater. Res. Express* **4**(10), 106106 (2017).
- ⁶¹P. Fischer, M. Polomska, I. Sosnowska, and M. Szymanski, *J. Phys. C Solid State Phys.* **13**(10), 1931 (1980).
- ⁶²P. S. V. Mocherla, C. Karthik, R. Ubic, M. S. R. Rao, and C. Sudakar, *Appl. Phys. Lett.* **103**(2), 022910 (2013).
- ⁶³S. Nandy, P. S. V. Mocherla, and C. Sudakar, *J. Appl. Phys.* **121**(20), 203102 (2017).
- ⁶⁴S. Nandy, K. Kaur, P. S. V. Mocherla, B. R. K. Nanda, and C. Sudakar, *J. Appl. Phys.* **124**(19), 195108 (2018).
- ⁶⁵S. V. M. Pavana, G. Sanjeev, C. Keun Hwa, M. S. R. Rao, and C. Sudakar, *Mater. Res. Express* **2**(9), 095012 (2015).
- ⁶⁶A. Gaur, P. Singh, N. Choudhary, D. Kumar, M. Shariq, K. Singh, N. Kaur, and D. Kaur, *Phys. B Condens. Matter* **406**(10), 1877–1882 (2011).
- ⁶⁷S. Logothetidis, *J. Appl. Phys.* **65**(6), 2416–2426 (1989).
- ⁶⁸Y. Zang, D. Xie, Y. Chen, X. Wu, G. Li, and D. Plant, *Integr. Ferroelectr.* **133**(1), 73–80 (2012).
- ⁶⁹C.-C. Huang, F. Al-Saab, Y. Wang, J.-Y. Ou, J. C. Walker, S. Wang, B. Gholipour, R. E. Simpson, and D. W. Hewak, *Nanoscale* **6**(21), 12792–12797 (2014).
- ⁷⁰E. Markiewicz, B. Hilczer, M. Błaszcyk, A. Pietraszko, and E. Talik, *J. Electroceram.* **27**(3), 154–161 (2011).
- ⁷¹H. Uchida, R. Ueno, H. Nakaki, H. Funakubo, and S. Koda, *Jpn. J. Appl. Phys.* **44**(18), L561–L563 (2005).
- ⁷²V. R. Palkar, J. John, and R. Pinto, *Appl. Phys. Lett.* **80**(9), 1628–1630 (2002).
- ⁷³A. H. M. Gonzalez, A. Z. Simões, L. S. Cavalcante, E. Longo, J. A. Varela, and C. S. Riccardi, *Appl. Phys. Lett.* **90**(5), 052906 (2007).
- ⁷⁴X. Tang, L. Jin, J. Dai, X. Zhu, and Y. Sun, *J. Alloys Compd.* **695**, 2458–2463 (2017).
- ⁷⁵R. Wang, H. Shu, W. Mao, X. Wang, H. Xue, L. Chu, J. Yang, and X. Li, *J. Supercond. Novel Magn.* **30**(4), 999–1002 (2017).
- ⁷⁶Y. Zhang, J. Qi, Y. Wang, Y. Tian, J. Zhang, T. Hu, M. Wei, Y. Liu, and J. Yang, *Ceram. Int.* **44**(6), 6054–6061 (2018).
- ⁷⁷K. P. Remya, S. Amirthapandian, M. M. Raja, C. Viswanathan, and N. Ponpandian, *J. Appl. Phys.* **120**(13), 134304 (2016).
- ⁷⁸S. Sharma, V. Singh, R. K. Dwivedi, R. Ranjan, A. Anshul, S. S. Amritphale, and N. Chandra, *J. Appl. Phys.* **115**(22), 224106 (2014).
- ⁷⁹R. P. Laughlin, D. A. Currie, R. Contreras-Guerro, A. Dedigama, W. Priyantha, R. Droopad, N. Theodoropoulou, P. Gao, and X. Pan, *J. Appl. Phys.* **113**(17), 17D919 (2013).
- ⁸⁰Y. Wang, Y. Lin, and C.-W. Nan, *J. Appl. Phys.* **104**(12), 123912 (2008).
- ⁸¹C.-J. Cheng, C. Lu, Z. Chen, L. You, L. Chen, J. Wang, and T. Wu, *Appl. Phys. Lett.* **98**(24), 242502 (2011).
- ⁸²F. Huang, X. Lu, W. Lin, Y. Kan, J. Zhang, Q. Chen, Z. Wang, L. Li, and J. Zhu, *Appl. Phys. Lett.* **97**(22), 222901 (2010).
- ⁸³K. Singh, S. K. Singh, and D. Kaur, *Ceram. Int.* **42**(12), 13432–13441 (2016).
- ⁸⁴X. Yan, G. Tan, W. Liu, H. Ren, and A. Xia, *Ceram. Int.* **41**(2, Pt. B), 3202–3207 (2015).
- ⁸⁵T.-J. Park, G. C. Papaefthymiou, A. J. Viescas, A. R. Moodenbaugh, and S. S. Wong, *Nano Lett.* **7**(3), 766–772 (2007).
- ⁸⁶P. S. V. Mocherla, D. Prabhu, M. B. Sahana, N. Y. Hebalkar, R. Gopalan, M. S. R. Rao, and C. Sudakar, *J. Appl. Phys.* **124**(7), 073904 (2018).
- ⁸⁷F. Huang, Z. Wang, X. Lu, J. Zhang, K. Min, W. Lin, R. Ti, T. Xu, J. He, C. Yue, and J. Zhu, *Sci. Rep.* **3**, 2907 (2013).
- ⁸⁸M. Alexe, *Nano Lett.* **12**(5), 2193–2198 (2012).